

FLOW BEHAVIOR AND CONSTITUTIVE MODEL OF A β - γ TiAl-BASED ALLOY UNDER HOT DEFORMATION

L. Xiang,^{a,1} B. Tang,^{b,c} J. Q. Tao,^a Q. Chen,^a Z. W. Huang,^a
G. Z. Zhao,^a Y. Liu,^b X. F. Chen,^b J. S. Li,^{b,c}
and Y. Tang^a

UDC 539.4

The flow behavior of a TNM alloy was evaluated in the high-temperature compression tests. The constitutive models for the flow curves and dynamic recrystallization were constructed to predict stress-strain and microstructure variations. The flow behavior of a Ti-43Al-4Nb-1Mo-0.2B alloy was studied by employing hot compression tests within a temperature range of 1000–1200°C and strain rates of 0.001–0.1 s⁻¹. The flow stress of the alloy was gradually going down with temperature and strain rate decrease, and dynamic recrystallization was the main softening mechanism. The peak shape evolution indicated that recrystallization occurred preferentially at high temperatures and low strain rates. The constitutive model for the flow behavior of the alloy was constructed with the fifth-order polynomial fitting method. Additionally, simulation of the volume fraction and grain sizes in recrystallization was effected. All the models demonstrated a good fit with the experimental results.

Keywords: flow behavior, TiAl-based alloy, constitutive model, hot deformation, dynamic recrystallization.

Introduction. The TiAl based alloys with low density, high specific yield strength, good oxidation resistance, and creep properties [1–3] are considered to be a promising candidate for manufacturing high-temperature structural materials in the aircraft and automotive industries [4–7]. Therefore, a lot of studies have been conducted on the microstructure evolution [8–11] and flow behavior [12, 13] of TiAl based alloy during high-temperature deformation, in order to make its application come true. Ti-(42-45)Al-(3-5)Nb-(0.1-2)Mo-(0.1-0.2)B alloy, referred as TNM alloy (all compositions are given in atomic percents (at.%) in the present study) was proposed by Clemens et al.[14–16], which is known to present an excellent high-temperature deformation ability. To date, the forging low-pressure turbine blades made of TNM alloy have been applied in Airbus A320neo [17].

Many metallurgical phenomena such as the dynamic recovery (DRV) and dynamic recrystallization (DRX) occur during hot deformation, which can be reflected through the variation of the flow curves [12, 13, 18]. Hence, it is greatly important to analyze and understand the flow behavior of alloys. Besides, the constitutive model can be deciphered by analyzing the flow curves of the metals, which is beneficial for predicting the flow behavior. The constitutive models for hot deformation of some typical alloys have been studied extensively [19–22]. However, only a few researchers focused their efforts on the TNM alloy. Therefore, it is necessary to study the constitutive model for TNM alloy. In the present study, the flow behavior of TNM alloy was studied using the high-temperature

^aSouthwest Technique and Engineering Institute, Chongqing, China (xlin0731@163.com). ^bState Key Laboratory of Solidification Processing, Northwestern Polytechnical University, Xi'an, Shaanxi, China. ^cNational & Local Joint Engineering Research Center for Precision Thermal Forming Technology of Advanced Metal Materials, Northwestern Polytechnical University, Xi'an, Shaanxi, China. Translated from Problemy Prochnosti, No. 1, pp. 163 – 172, January – February, 2021. Original article submitted January 15, 2020.

TABLE 1. Actual Chemical Composition of the TNM Alloy (at.%)

Ti	Al	Nb	Mo	B	Fe	C	O
Bal.	42.92	4.01	0.99	0.18	0.03	0.03	0.11

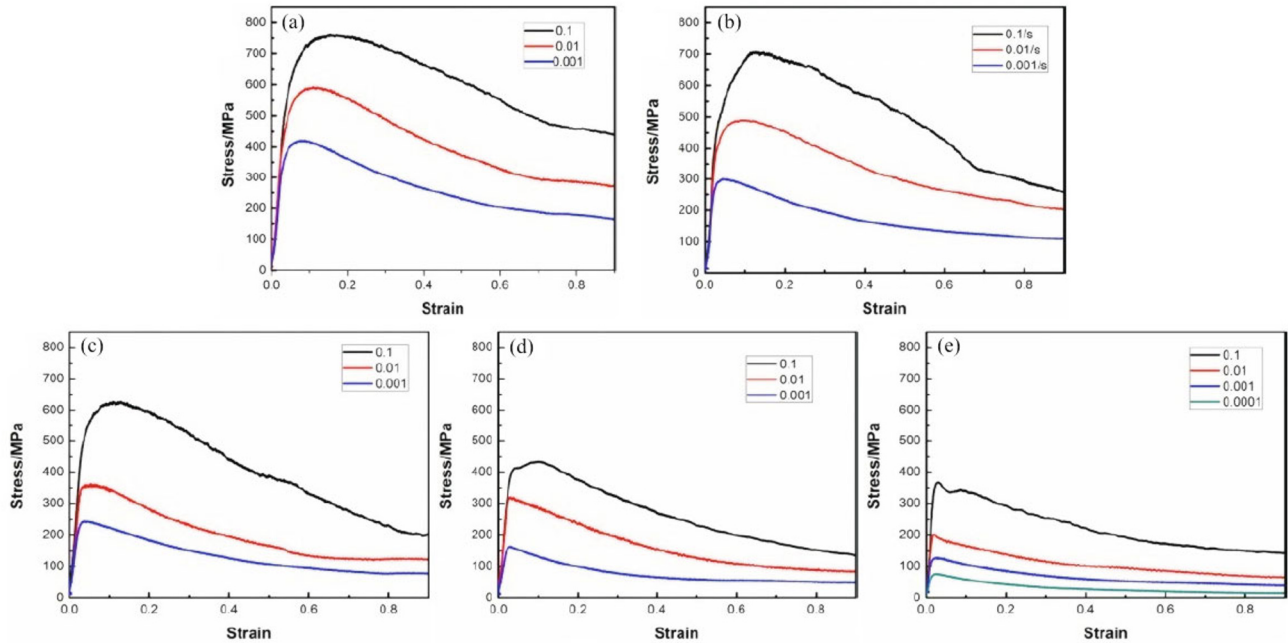


Fig. 1. Flow curves of TNM alloy at various deformation conditions: (a) 1000°C; (b) 1050°C; (c) 1100°C; (d) 1150°C; (e) 1200°C.

compression tests. Subsequently, the constitutive model for flow curves and DRX were established to predict the variation of the stress-strain and microstructure.

1. Material and Experimental. TNM alloy ingot with a nominal composition of Ti-43Al-4Nb-1Mo-0.2B was fabricated using the triple vacuum arc re-melting (VAR) method, following by hot iso-static pressing (HIPing) at 1280°C for 4 h under a pressure of 140 MPa. Subsequently, the electric-discharge machining was employed to cut the hot compression specimens with a dimension of $\varnothing 8 \times 12$ mm from the ingot. The initial microstructure of TNM alloy was reported previously [18], and the actual composition is shown in Table 1. High-temperature compression tests were conducted using a Gleeble 3500 Thermo-simulation machine at temperatures of 1000, 1050, 1100, 1150, and 1200°C and strain rates of 10^{-1} , 10^{-2} , and 10^{-3} s $^{-1}$ under a true strain of 0.9. In order to reduce the friction between specimen and machine and acquire the true stress–strain curve, a graphite lubricant was painted on the sides of the specimens and the pressure heads of the machine. Subsequently, the compressive specimens were heated up to the deformation temperature at a rate of 10 K/s under a vacuum and soaked for 5 min immediately after the heating was over. When the target strain was achieved, the compressive specimens were quenched immediately. A previous report [23] was employed to modify the effect of friction between the specimen and the machine in all the obtained flow curves.

2. Results and Discussion.

2.1. Flow Behavior of TNM Alloy. Figure 1 shows the flow curves of the present alloy at different deformation temperatures and strain rates under a true strain of 0.9. There are four typical features in Fig. 1. The first feature is that flow stress increased significantly with an increase in the strain at the initial stage before reaching the peak value, after which the flow stress gradually decreased till a steady-state regime was achieved. The second feature is that all flow curves presented only one peak. The third feature is that the curvilinear peaks of the specimens deformed at low temperature and high strain rate were smooth, while those at high temperature and low strain rate

TABLE 2. Peak Strains under Different Deformation Conditions

Deformation conditions (s^{-1})	1000°C	1050°C	1100°C	1150°C	1200°C
0.1	0.15405	0.12619	0.12907	0.09920	0.02958
0.01	0.10977	0.09129	0.05316	0.03104	0.02050
0.001	0.07281	0.04340	0.03779	0.02992	0.02800

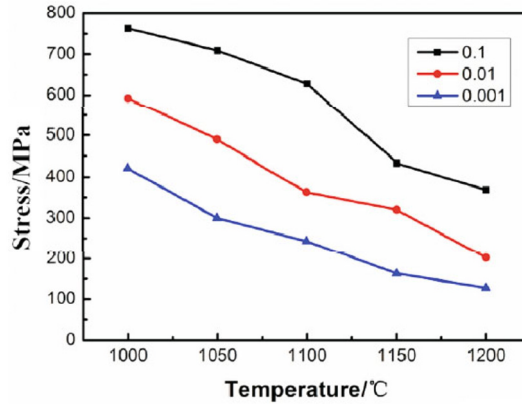


Fig. 2. Relationship between the peak stress and temperature.

were very sharp. The fourth feature is that the flow curves of specimens deformed at high temperature and low strain rate reached the steady-state regime faster than those at the opposite deformation conditions.

It is well-known that the DRX, DRV, and work hardening usually happens during the hot deformation [24, 25]. DRX is easy to occur in TiAl based alloy due to the low stack fault energy [26, 27]. At the initial stage of deformation, a lot of dislocations were induced and propagated with the increase in the strain in the TNM alloy, which winded each other and pinned by grain boundaries, leading to the increase in the stress. After reaching a critical strain, DRX was triggered, leading to a consumption of a lot of dislocations. Accordingly, flow stress decreased with a disappearance of the dislocations, i.e., the flow curve reached the softening stage. At this stage, the deformation-induced dislocation was continuously consumed by DRX. When equilibrium between the propagation and consumption of the dislocation was built, the flow curve reached the steady-state regime. Therefore, all flow curves in Fig. 1 show only one peak. Besides, the flow strain curves were showed that the higher temperature and lower strain rate led to the smaller critical stress, which meant softening mechanism was easier to occur. On the one hand, the temperature provided the essential deformable energy for the nucleation and the growth of DRX. On the other hand, when specimens deformed at low strain rate, a sufficient deformation time ensured the occurrence of DRX, thereby leading to a decrease in the flow stress.

The relationship between the peak stress and temperature is presented in Fig. 2. It was found that the peak stress decreased linearly an increase in the deformation temperature. Table 2 shows the peak strains of flow curves under various deformation conditions. The peak strains gradually decreased with increasing temperatures and decreasing strain rates, i.e., the strain for the softening stage decreased. This indicated that the DRX of the present alloy preferred to occur at high temperature and low strain rate, leading to no transition stage in the flow curves, which is the reason for the third feature. A similar result obtained by the microstructural analysis was published in [18].

2.2. Model for Flow Curves. The variation of the stress with deformation parameters can be described by the Arrhenius equation [28, 29] to understand the hot deformation behavior of materials, as shown in Eqs. (1)–(3):

$$Z = \dot{\epsilon} \exp(Q/RT) = A[\sinh(\alpha\sigma)]^n, \quad (1)$$

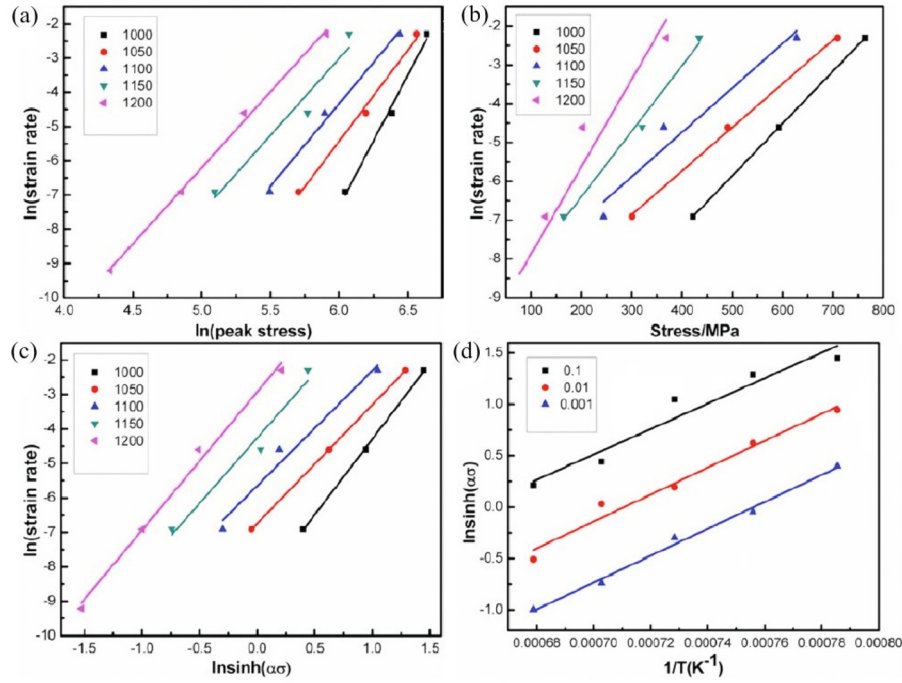


Fig. 3. Relationship of σ , $\dot{\epsilon}$, and T : (a) relationship between $\ln \dot{\epsilon}$ and $\ln \sigma$; (b) relationship between $\ln \dot{\epsilon}$ and σ ; (c) relationship between $\ln \dot{\epsilon}$ and $\ln[\sinh(\alpha\sigma)]$; (d) relationship between $\ln[\sinh(\alpha\sigma)]$ and $1/T$.

$\alpha\sigma < 0.8$,

$$\dot{\epsilon} = B\sigma^{n'}, \quad (2)$$

$\alpha\sigma > 1.2$,

$$\dot{\epsilon} = B' \exp(\beta\sigma), \quad (3)$$

where n and n' are the stress exponents, Q is the activation energy (J/mol), T is the absolute temperature (K), α , A , β , B , and B' are material constants, R is the gas constant, and Z is the Zener–Hollomon constant. A relationship between α , β , and n' exists as $\alpha = \beta/n'$.

The value of β and n' can be obtained from the relationships of $\ln(\text{strain rate}) - \ln(\text{stress})$ and $\ln(\text{strain rate}) - \text{stress}$, as plotted in Fig. 3a and 3b, i.e., $n' = 5.355776$, $\beta = 0.01511$. Thus, the material constant α of the present alloy was $2.821253 \cdot 10^{-3}$. The activation energy Q can be determined by Eq. (4):

$$Q = R \left\{ \frac{\partial \ln \dot{\epsilon}}{\partial \ln[\sinh(\alpha\sigma)]} \right\}_T \left\{ \frac{\partial \ln[\sinh(\alpha\sigma)]}{\partial (1/T)} \right\}_{\dot{\epsilon}}. \quad (4)$$

Similarly, the value of $\left\{ \frac{\partial \ln \dot{\epsilon}}{\partial \ln[\sinh(\alpha\sigma)]} \right\}_T$ and $\left\{ \frac{\partial \ln[\sinh(\alpha\sigma)]}{\partial (1/T)} \right\}_{\dot{\epsilon}}$ can be calculated by Fig. 3c and 3d. Thus,

the activation energy Q of the present alloy was 404.86 kJ/mol, which was significantly higher than the Ti self-diffusion (250 kJ/mol) and Al self-diffusion (360 kJ/mol) in single γ -TiAl alloy [30, 31]. Such a high value of Q indicated that the main softening mechanism of TNM alloy was DRX, which matched with the above analysis of the flow curves. This was also proved in our previous work on the corresponding microstructure [18].

Taking the logarithm of both sides of Eq. (1), the material constants of Z can be expressed by Eq. (5):

$$\ln(Z) = \ln A + n \ln[\sinh(\alpha\sigma)]. \quad (5)$$

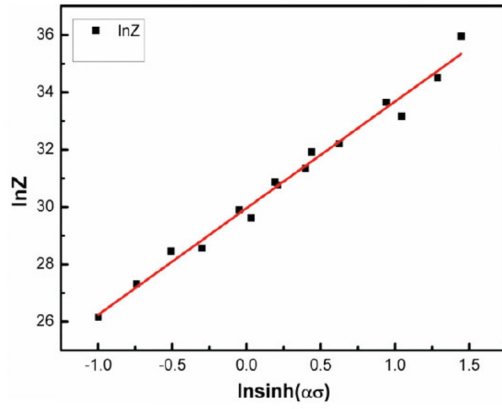


Fig. 4. Relationship between $\ln Z$ and $\ln[\sinh(\alpha\sigma)]$.

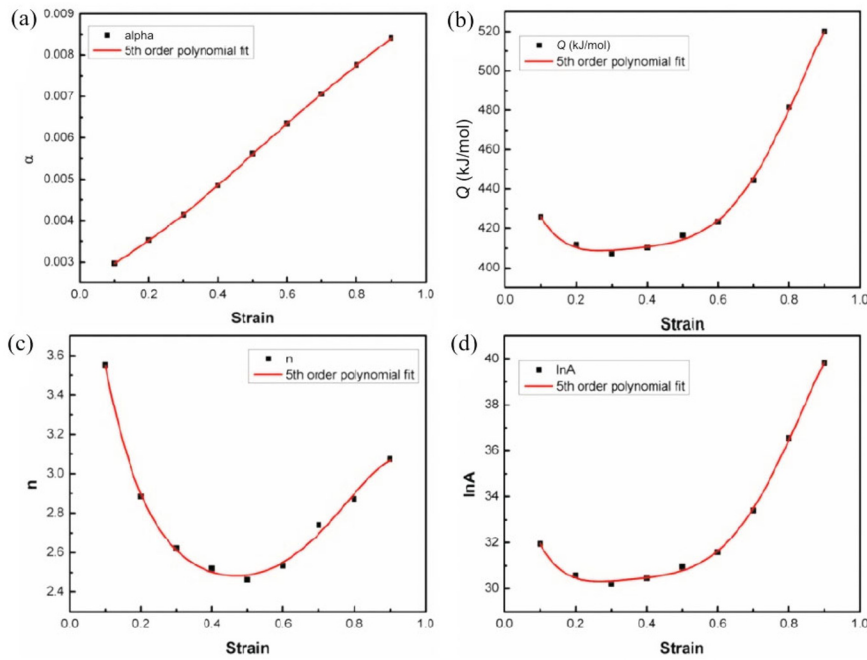


Fig. 5. Relationship between the material constants and strain.

The relationship between the constant Z and the peak stress σ is shown in Fig. 4. Through linear fitting, the value of constant A and n were found to be $1.02 \cdot 10^{13}$ and 3.71, respectively.

From Eq. (1), it can be found that the flow stress was related to material constants of α , n , A , and Q , as shown in Eq. (6):

$$\sigma = \frac{1}{\alpha} \ln \left\{ \left(\frac{Z}{A} \right)^{1/n} + \left[\left(\frac{Z}{A} \right)^{2/n} + 1 \right]^{0.5} \right\}. \quad (6)$$

It can be thus found that the constants α , n , A , and Q were significantly influenced by stress corresponding to strain, i.e., the value of constants α , n , A , and Q changed with a variation in the strain. Hence, the variation of the material constants with strain should be taken into account to establish the constitutive model. This work employed the fifth polynomial fitting method to find the relationship between the material constants and strain, in order to predict the flow stress accurately (shown in Fig. 5). It can be found that material constants n , $\ln A$, and Q

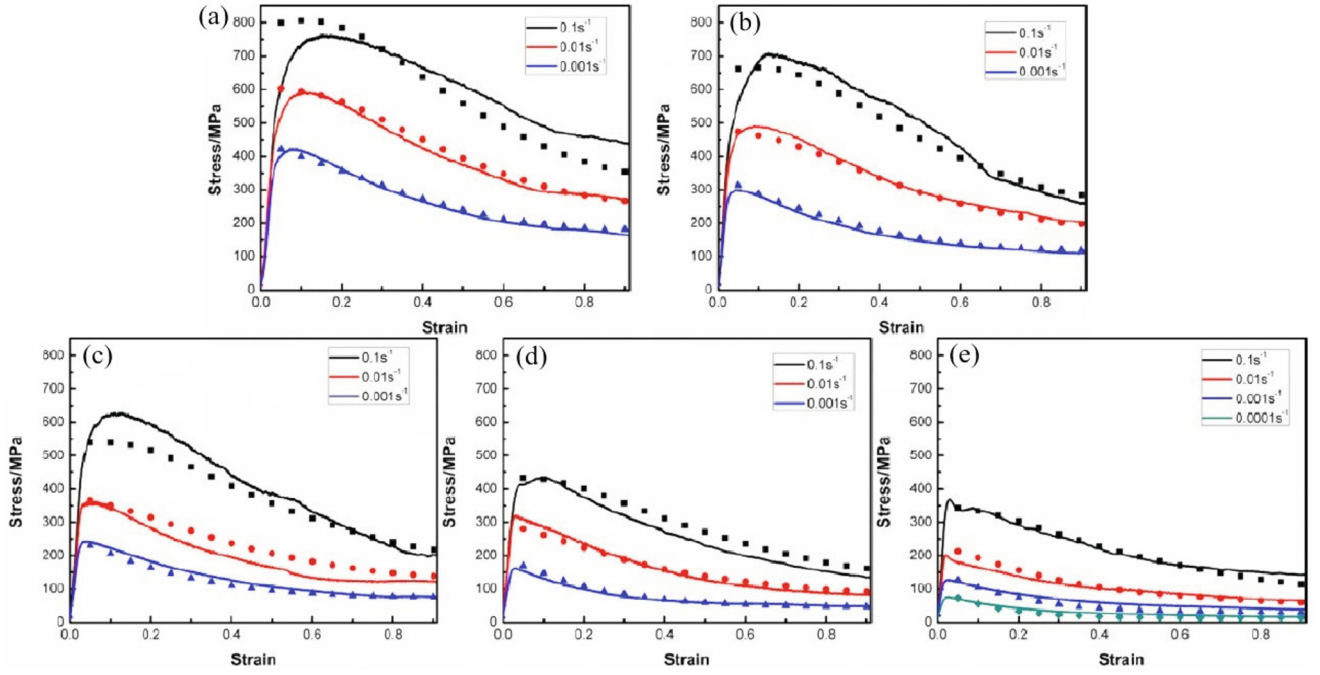


Fig. 6. Comparison between the experimental and the predicted results: (a) 1000°C; (b) 1050°C; (c) 1100°C; (d) 1150°C; (e) 1200°C. (Solid line and data points represent experimental flow stress and predicted flow stress, respectively.)

decreased initially and then gradually increased with strain. However, the material constant α increased nearly linearly, with an increase in the strain. The relationships between material constants and strain are expressed in the following equations:

$$\alpha = 0.00248 + 0.00482\varepsilon - 6.33502 \cdot 10^{-4}\varepsilon^2 + 0.01734\varepsilon^3 - 0.02671\varepsilon^4 + 0.01185\varepsilon^5, \quad (7)$$

$$Q = 483.08 - 908.96\varepsilon + 4263.11\varepsilon^2 - 9567.87\varepsilon^3 + 10234.11\varepsilon^4 - 3958.49\varepsilon^5, \quad (8)$$

$$n = 4.90329 - 18.69539\varepsilon + 61.21009\varepsilon^2 - 108.03154\varepsilon^3 + 100.65969\varepsilon^4 - 37.05013\varepsilon^5, \quad (9)$$

$$\ln A = 37.2562 - 84.5311\varepsilon + 395.5132\varepsilon^2 - 885.2878\varepsilon^3 + 944.1296\varepsilon^4 - 365.4192\varepsilon^5. \quad (10)$$

Figure 6 shows the comparison between the experimental and the predicted results. The predicted results were close to the experimental results, at most of the deformation conditions. A few specimens deformed at low temperature and high strain rate, in which the predicted results showed a deviation from the experimental results due to cracking of the specimens. Therefore, the constitutive model in this work could predict the flow curves of TNM alloy with high accuracy.

2.3. Model for Dynamic Recrystallization. From earlier reports [8, 9], DRX is known to be the main softening mechanism for TNM alloy. The volume fraction of DRX can be expressed by Avrami type equation:

$$X_{DRX} = 1 - \exp \left[-k \left(\frac{\varepsilon - \varepsilon_c}{\varepsilon_{0.5}} \right)^n \right], \quad (11)$$

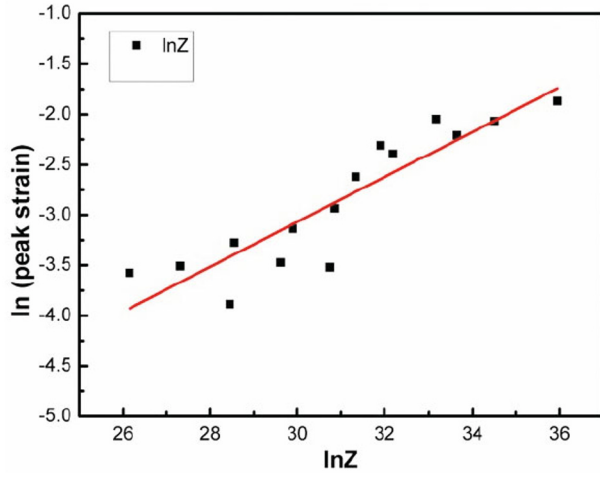


Fig. 7

Fig. 7. Relationship between peak strain and Zener–Hollomon constant.

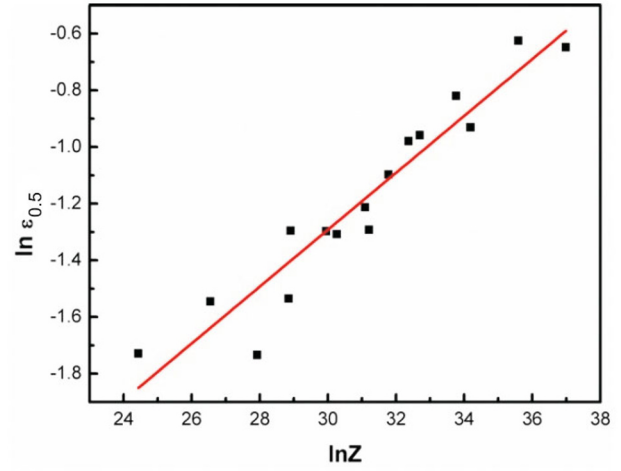


Fig. 8

Fig. 8. Relationship between $\varepsilon_{0.5}$ and Zener–Hollomon constant.

where X_{DRX} is the volume fraction of DRX, n is Avrami exponent, k is material constant, and ε , ε_c , and $\varepsilon_{0.5}$ are strain, critical strain and the strain of volume fraction of DRX is 50%, respectively. For TiAl-based alloy, many reports demonstrate that the critical strain was close to the peak strain [32]. Hence, the peak strain was taken to replace the critical strain in this work. Meanwhile, the volume fraction of DRX also can be represented as

$$X_{DRX} = \frac{\sigma_p - \sigma}{\sigma_p - \sigma_s}, \quad (12)$$

where σ_p and σ_s are the peak stress and steady-state stress, respectively.

Figure 7 shows the relationship between the peak strain and $\ln Z$, which showed a linear relation. Therefore, the peak strain can be expressed by a function of $\ln Z$ as

$$\varepsilon_p = 5.758 \cdot 10^{-5} Z^{0.22311}. \quad (13)$$

Similarly, the relationship between $\varepsilon_{0.5}$ and $\ln Z$ is shown in Fig. 8. The corresponding function also can be obtained as follows:

$$\varepsilon_{0.5} = 1.35336 \cdot 10^{-2} Z^{0.10036}. \quad (14)$$

Figure 9 shows the comparison between the recrystallization fraction model and the experimental results. It is obvious that a good fitting existed between the predicted results and the experimental results. Meanwhile, there are three stages in Fig. 9. In the first and third stages, the volume fraction of DRX increased slowly, with increasing strain. However, the volume fraction of DRX increased significantly with strain in the second stage. The curves presented an “S” shape. Besides, the first stage was shortened and the increasing tendency of X_{DRX} was more intensive at high temperatures, as shown in Fig. 9b. These phenomena indicate that the high temperature was beneficial for the occurrence of DRX, which corresponded well to the above analysis results.

For TNM alloy, DRX was easy to occur during hot deformation. Hence, it was important to establish modeling for grain size of DRX. The grain size of DRX exhibited an inverse relation with Zener–Hollomon constant [33] as

$$d_{DRX} = kZ^{-N}, \quad (15)$$

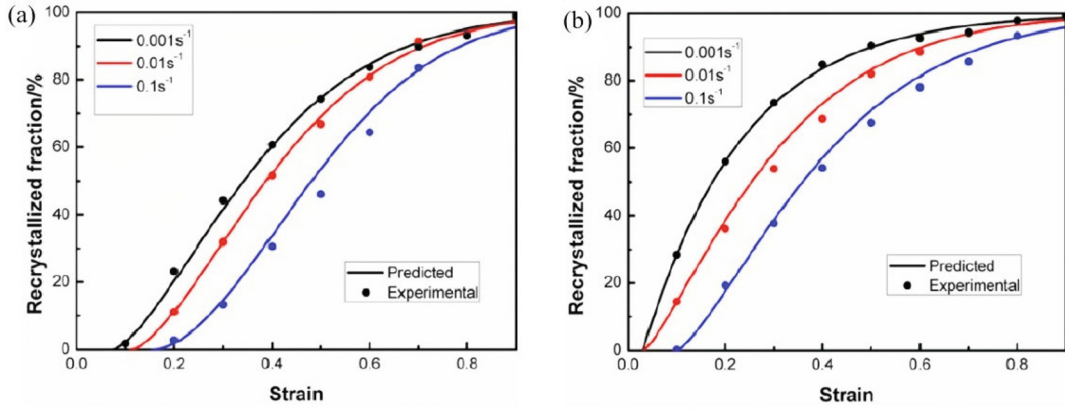


Fig. 9. Comparison between recrystallization fraction model and experimental results: (a) 1000°C; (b) 1150°C.

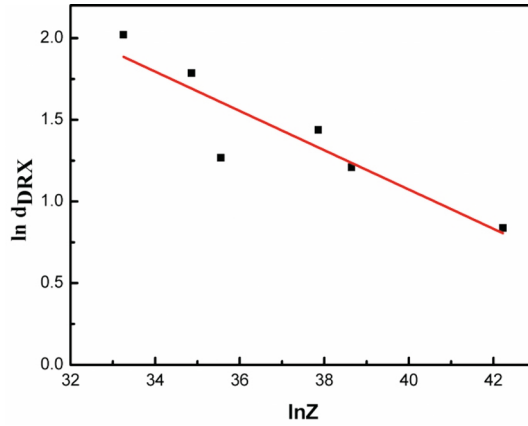


Fig. 10. Relationship between the recrystallization grain size and Zener–Hollomon constant.

where k and N are material constants. Data of grain size were obtained in the central microstructure of deformed specimens through EBSD technique, and the relationship between the size of DRX grain and Zener–Hollomon constant is shown in Fig. 10. Therefore, modeling of the DRX grain size is

$$d_{DRX} = 359.92Z^{-0.12032}. \quad (16)$$

According to Eq. (1), Z was related to the activation energy Q , changing with strain. So, modeling for size of DRX grain was revised as follows:

$$d_{DRX} = 359.92Z^{-0.12032},$$

$$Z = \dot{\epsilon} \exp(Q/RT),$$

$$Q = 483.08 - 908.96\epsilon + 4263.11\epsilon^2 - 9567.87\epsilon^3 + 10234.11\epsilon^4 - 3958.49\epsilon^5.$$

Conclusions. In the present study, the flow behavior of TNM alloy was studied using hot compression tests at 1000–1200°C and 0.001–0.1 s⁻¹, and corresponding constitutive models were established. The main conclusions of the study are as follows:

1. Only one peak in all flow curves with smooth shape existed at a low temperature and high strain rate. However, it was sharp at high temperatures and low strain rates. This indicated that DRX was easier to occur, and the softening ability was stronger at high temperatures and low strain rates.

2. Constitutive model for flow behavior of TNM alloy was established using the fifth polynomial fitting method and considering the variation in the material constants, which predicted the flow curves accurately.

3. Models were established for the volume fraction of DRX, and DRX grain size was established. The DRX model showed a good fitting with the experimental results. The variation in the activation energy with strain was taken into consideration during the modeling for DRX grain size.

Acknowledgments. This work was financially supported by the National Natural Science Foundation of China (No. 51771150), the Natural Science Basic Research Project of Shaanxi (No. 2018JM5174), and the Research Fund of the State Key Laboratory of Solidification Processing (NPU), China (Grant No. 2019-TS-07).

REFERENCES

1. F. Appel, U. Brossmann, U. Christoph, et al., "Recent progress in the development of gamma titanium aluminide alloys," *Adv. Eng. Mater.*, **2**, 699–720 (2000).
2. H. Clemens and H. Kestler, "Processing and applications of intermetallic γ -TiAl-based alloys," *Adv. Eng. Mater.*, **2**, 551–570 (2000).
3. E. A. Loria, "Gamma titanium aluminides as prospective structural materials," *Intermetallics*, **8**, 1339–1345 (2000).
4. X. Wu, "Review of alloy and process development of TiAl alloys," *Intermetallics*, **14**, 1114–1122 (2006).
5. S. W. Kim, J. K. Hong, Y. S. Na, et al., "Development of TiAl alloys with excellent mechanical properties and oxidation resistance," *Mater. Design*, **54**, 814–819 (2014).
6. R. A. Harding, M. Wickins, H. Wang, et al., "Development of a turbulence-free casting technique for titanium aluminides," *Intermetallics*, **19**, 805–813 (2011).
7. W. J. Zhang, U. Lorenz, and F. Appel, "Recovery, recrystallization and phase transformations during thermomechanical processing and treatment of TiAl-based alloys," *Acta Mater.*, **48**, 2803–2813 (2000).
8. J. B. Li, Y. Liu, Y. Wang, et al., "Dynamic recrystallization behavior of an as-cast TiAl alloy during hot compression," *Mater. Charact.*, **97**, 169–177 (2014).
9. C. L. Chen, W. Lu, D. Sun, et al., "Deformation induced $\alpha_2 \rightarrow \gamma$ phase transformation in TiAl alloys," *Mater. Charact.*, **61**, 1029–1034 (2010).
10. L. Cheng, H. Chang, B. Tang, et al., "Deformation and dynamic recrystallization behavior of a high Nb containing TiAl alloy," *J. Alloy. Compd.*, **522**, 363–369 (2013).
11. N. Cui, F. T. Kong, X. P. Wang, et al., "Hot deformation behavior and dynamic recrystallization of a β -solidifying TiAl alloy," *Mater. Sci. Eng. A*, **652**, 231–238 (2016).
12. S. Z. Zhang, C. J. Zhang, Z. X. Du, et al., "Microstructure and tensile properties of hot forged high Nb containing TiAl based alloy with initial near lamellar microstructure," *Mater. Sci. Eng. A*, **642**, 16–21 (2015).
13. L. Xiang, B. Tang, X. Y. Xue, et al., "Characteristics of dynamic recrystallization behavior of Ti-45Al-8.5Nb-0.2W-0.2B-0.3Y alloy during high temperature deformation," *Metals*, **7**, 261 (2017).
14. H. Clemens, H. F. Chladi, W. Wallgram, et al., "In and ex situ investigations of the β -phase in a Nb and Mo containing γ -TiAl based alloy," *Intermetallics*, **16**, 827–833 (2008).
15. E. Schwaighofer, H. Clemens, J. Lindemann, et al., "Hot-working behavior of an advanced intermetallic multi-phase γ -TiAl based alloy," *Mater. Sci. Eng. A*, **614**, 297–310 (2014).
16. E. Schwaighofer, H. Clemens, S. Mayer, et al., "Microstructural design and mechanical properties of a cast and heat-treated intermetallic multi-phase γ -TiAl based alloy," *Intermetallics*, **44**, 128–140 (2014).
17. P. Janschek, "Wrought TiAl blades," *Mater. Today-Proc.*, **2**, 92–97 (2015).
18. L. Xiang, B. Tang, X. Y. Xue, et al., "Microstructural characteristics and dynamic recrystallization behavior of β - γ TiAl based alloy during high temperature deformation," *Intermetallics*, **97**, 52–57 (2018).
19. S. S. Li, X. K. Su, Y. F. Han, et al., "Simulation of hot deformation of TiAl based alloy containing high Nb," *Intermetallics*, **13**, 323–328 (2005).

20. B. Liu, Y. Liu, W. Zhang, and J. S. Huang, "Hot deformation behavior of TiAl alloys prepared by blended elemental powders," *Intermetallics*, **19**, 1184–1190 (2011).
21. H. Mirzadeh, J. M. Cabrera, and A. Najafizadeh, "Constitutive relationship for hot deformation of austenite," *Acta Mater.*, **59**, 6441–6448 (2011).
22. X. P. Liang, Y. Liu, H. Z. Li, et al., "Constitutive relationship for high temperature deformation of powder metallurgy Ti-47Al-2Cr-2Nb-0.2W alloy," *Mater. Design*, **37**, 40–47 (2012).
23. L. Cheng, H. Chang, B. Tang, et al., "Flow stress prediction of high-Nb TiAl alloys under high temperature deformation," *Adv. Mater. Res.*, **510**, 723–728 (2012).
24. L. Huang, P. K. Liaw, Y. Liu, and J. S. Huang, "Effect of hot-deformation on the microstructure of the Ti-Al-Nb-W-B alloy," *Intermetallics*, **28**, 11–15 (2012).
25. H. Z. Niu, Y. Y. Chen, F. T. Kong, and J. P. Lin, "Microstructure evolution, hot deformation behavior and mechanical properties of Ti-43Al-6Nb-1B alloy," *Intermetallics*, **31**, 249–256 (2012).
26. F. Appel, M. Oehring, and R. Wagner, "Novel design concepts for gamma-base titanium aluminide alloys," *Intermetallics*, **8**, 1283–1312 (2000).
27. L. Cheng, X. Y. Xue, B. Tang, et al., "Flow characteristics and constitutive modeling for elevated temperature of a high Nb containing TiAl alloy," *Intermetallics*, **49**, 23–28 (2014).
28. Y. Cao, H. Di, J. Zhang, et al., "An electron backscattered diffraction study on the dynamic recrystallization behavior of a nickel-chromium alloy (800H) during hot deformation," *Mater. Sci. Eng. A*, **585**, 71–85 (2013).
29. R. Bobbili, B. V. Ramudu, and V. Madhu, "A physically-based constitutive model for hot deformation of Ti-10-2-3 alloy," *J. Alloy. Compd.*, **696**, 295–303 (2017).
30. C. Herzig, T. Przeorski, and Y. Mishin, "Self-diffusion in γ -TiAl: an experimental study and atomistic calculations," *Intermetallics*, **7**, 389–404 (1999).
31. Y. Mishin and C. Herzig, "Diffusion in the Ti-Al system," *Acta Mater.*, **48**, 589–623 (2000).
32. S. Kim and Y. C. Yoo, "Dynamic recrystallization behavior of AISI 304 stainless steel," *Mater. Sci. Eng. A*, **311**, 108–113 (2001).
33. G. R. Ebrahimi, A. R. Maldara, R. Ebrahimi, and A. Davoodi, "Effect of thermomechanical parameters on dynamically recrystallized grain size of AZ91 magnesium alloy," *J. Alloy. Compd.*, **509**, 2703–2708 (2011).